JAMES | Journal of Advances in Modeling Earth Systems

RESEARCH ARTICLE
10.1029/2018MS001521

The Modeling of the North Equatorial Countercurrent in the Community Earth System Model and its Oceanic Component

Zhikuo Sun[1,2], Hailong Liu[1,2], Pengfei Lin[1,2], Yu-heng Tseng[3], Justin Small[4], and Frank Bryan[4]

[1]State Key Laboratory of Numerical Modeling for Atmospheric Sciences and Geophysical Fluid Dynamics (LASG), Institute of Atmospheric Physics, Chinese Academy of Sciences, Beijing, China, [2]College of Earth and Planetary Sciences, University of Chinese Academy of Sciences, Beijing, China, [3]Institute of Oceanography, National Taiwan University, Taipei, Taiwan, [4]National Center for Atmospheric Research, Boulder, CO, USA

Key Points:
- The NECC transport is underestimated in the POP west of 120°W and it is underestimated in the CESM east of 120°W
- West of 120°W, the POP's NECC bias comes from the southward movement of the easterly trade winds and WSC pattern in the northern hemisphere
- East of 120°W, the NECC biases in the CESM mainly attribute to the weak cross-equatorial southerly winds and northeasterly gap winds

Correspondence to:
H. Liu and Y.-h. Tseng,
lhl@lasg.iap.ac.cn;
tsengyh@ntu.edu.tw

Citation:
Sun, Z., Liu, H., Lin, P., Tseng, Y.-h., Small, J., & Bryan, F. (2019). The modeling of the North Equatorial Countercurrent in the Community Earth System Model and its oceanic component. *Journal of Advances in Modeling Earth Systems*, *11*, 531–544. https://doi.org/10.1029/2018MS001521

Received 10 OCT 2018
Accepted 17 JAN 2019
Accepted article online 21 JAN 2019
Published online 20 FEB 2019

Abstract The North Equatorial Countercurrent (NECC) simulated by a coupled ocean-atmosphere model and its oceanic component have been investigated and compared against oceanographic observations. Coupled model simulations using the Community Earth System Model version 2 are compared against ocean-ice simulations forced by the second phase of the Coordinated Ocean-ice Reference Experiments (CORE) data set. The modeled circulation biases behave differently to the west of and to the east of 120°W: the CORE-forced ocean model largely underestimates the NECC transport to the west and the coupled model underestimates it to the east. Further analysis suggests that the surface wind stress and its curl is the most important forcing term for correctly simulating the NECC in both models. West of 120°W, the NECC biases in the ocean model are attributed to the southward movement of the maximum easterly trade winds in the Northern Hemisphere and the associated wind stress curl (WSC) pattern; east of 120°W, the NECC biases in the coupled model are attributed to the weak northward cross-equatorial winds and southwestward gap winds, which lead to a weak WSC gradient at the latitude of NECC. Further analysis confirms that the WSC biases comes mainly from the zonal wind bias, which may in turn relate to the protocol of CORE-II of adjusting reanalysis winds toward satellite data, which include the relative wind effect.

1. Introduction

The North Equatorial Countercurrent (NECC) is a major upper-ocean zonal flow of the wind-driven circulation in the tropical Pacific, flowing eastward across the Pacific Ocean basin between 2°N and 10°N. The main body of NECC shifts poleward as it flows to the east; located near 5°N in the western Pacific and shifted to 7°N in the central Pacific (Donguy & Meyers, 1996; Johnson et al., 2002; Wyrtki & Kendall, 1967). The vertical extent of the NECC also changes as it crosses the Pacific: shallower in the west and deeper in the east. On average, the NECC transport is about 10–30 Sv eastward out of the warm pool region to the relatively cold eastern Pacific. The maximum value of zonal velocity of the NECC can reach 0.4 m/s near 220°E (Gouriou & Toole, 1993; Johnson et al., 2002; Wyrtki & Kendall, 1967). The NECC plays important roles in the volume and heat budget of the warm pool (Clement et al., 2005; Meyers & Donguy, 1984; Picaut & Delcroix, 1995) and in shaping the tropical Pacific climate (e.g., Masunaga & L'Ecuyer, 2011).

The classical Sverdrup dynamics and also nonlinear processes are involved in the NECC physics (Kessler et al., 2003; Sverdrup, 1947; Yu et al., 2000). The eastward flow counter to the wind direction is mainly due to the vorticity imposed by the wind stress curl (WSC). Kessler et al. (2003) also investigated the effects of other terms, such as the advection and friction, on the NECC transport. In their study, although the advection and friction terms are small, their meridional derivatives are large enough to contribute to balancing the vorticity input by WSC. The zonal transport due to the advection and friction can effectively reduce the wind-driven NECC transport, especially in the western equatorial Pacific.

It has been found that the NECC is not well simulated in many ocean models partly because of these complex dynamics (e.g., Grima et al., 1999; Philander et al., 1987; Tseng et al., 2016; Wu et al., 2012). In the recent second phase of the Coordinated Ocean-ice Reference Experiments (CORE-II), the NECC simulated in the stand-alone ocean models generally tend to be weak (Tseng et al., 2016, their Figure 19). The climatological

mean zonal current speeds of the NECC from 15 different ocean models are all less than half of the observational estimate of 0.4 m/s (Johnson et al., 2002) at 220°E. Even the high-resolution KIEL model shows similar weak velocity magnitude. Although Tseng et al. (2016) identified the systematic model biases from the CORE-II models and found that the systematic error may come mainly from the surface wind stress curl in the tropic, they did not further investigate the fundamental causes.

The biases in the NECC are usually attributed to the surface wind forcing, both locally and at the equator (Wu et al., 2012; Yu et al., 2000). Yu et al. (2000) pointed out that the strong surface wind at the equator would lead to a shift in the NECC near the date line. Based on two ocean model simulations, Wu et al. (2012) suggested that biases in satellite surface wind estimates associated with the southward shift of the Intertropical Convergence Zone (ITCZ) would yield a weak NECC. Richards et al. (2009) also found modest changes in the strength of the NECC associated with a change in the ocean diffusivity in a regional coupled model and attributed it to a change in wind stress curl, via an indirect effect of changing the sea surface temperature. Therefore, the surface winds from CORE-II data in the Tropical Pacific are likely the primary cause of the model biases. However, which part of the winds is responsible for the biases? Are there other processes than the surface winds contributing to the weak biases in the NECC simulation? Those questions have not been systemically investigated yet.

In stark contrast, several Community Earth System Model version 2 (CESM2) model simulations (regardless of resolution) show more realistic NECC strengths than the results from simulations with the same ocean component model (Parallel Ocean Program version 2, POP2) forced by wind stress derived from observations. Why is the NECC in the coupled model simulated better than that in the stand-alone ocean model? Can the wind stress distribution in the coupled model be a more accurate depiction of the real condition than the analyses in CORE-II? Here the results from the fully coupled model serve as a reference to the stand-alone ocean models, in particular, for the vorticity balance analysis.

The purpose of the present paper is to investigate the impacts of surface wind stresses and other terms on the representation of the NECC in simulations with the POP2 ocean model, both forced with CORE-II atmospheric observations and coupled to an atmospheric model in CESM2. Our results should help us to understand the dynamical processes involved in the model biases which can potentially help in future development of methods for forcing stand-alone ocean models.

2. Models, Experiments, and Observation Data

In the present study, the CESM2 framework developed at the National Center for Atmospheric Research (NCAR) is used. The ocean component of CESM2 is the POP2, which has 60 vertical levels, monotonically increasing from 10 m near the surface to 250 m in the deep ocean. POP2 uses a displaced North Pole grid with a nominal 1° horizontal resolution. Near the equator, the meridional resolution is increased to 0.27° (Danabasoglu et al., 2014). The sea ice component is sea ice model version 5 (CICE5). The atmospheric component of CESM2 is the version 6.0 of the Community Atmosphere Model (CAM6) with a finite volume nominal resolution of 1° (0.9° × 1.25°) and 30 vertical levels. The land model is the Community Land Model version 5 (CLM5) for the CESM2. The details of CLM5 can be found in the official website of CESM2.

The interannual forcing data set (CORE-IAF.v2) is used in the following experiments, developed by Large and Yeager (2004, 2009) and based on surface atmospheric fields derived from National Centers for Environmental Prediction (NCEP)/NCAR atmospheric reanalysis (Kistler et al., 2001) and radiation and precipitation and runoff from other sources (Large & Yeager, 2009). The surface atmospheric fields are adjusted with respect to available observations to reduce the biases and uncertainties in the reanalysis fields. For winds, the time average of the QuikSCAT (QuikScat scatterometer) data set is used to correct the NCEP wind speed and adjust the wind direction. The magnitude and angle of the wind vector were adjusted by a multiplicative factor $R_s(\lambda,\phi)$ and a counterclockwise rotating factor $\delta(\lambda,\phi)$, respectively, where λ and ϕ, respectively, represent longitude and latitude. The main consideration is to match the mean wind speed and mean wind direction from QuikSCAT everywhere (Large & Yeager, 2009).

Three experiments have been used in the present study: (i) a standard CORE-II ocean-ice experiment (POP2 coupled to CICE5), which is forced by the CORE-II interannual forcing data set (hereafter referred to as the "POP" experiment); here, the POP was run for 60 years using CORE-II interannual forcing data set

(1948–2009) following 260 years of spin-up and the solution during 1978–2007 are used for the analysis; (ii) additionally an ocean ice simulation forced by the modified CORE-II interannual forcing data set, without correction to NCEP winds based on QuikSCAT (referred to as the "POP-UNCO" experiment). The initial conditions of these two POP experiments are the January (winter) climatology from World Ocean Atlas 2013 version 2. (iii) The third simulation is a preindustrial run of CESM2 (referred to as the "CESM" experiment), which is set up for the estimated 1850 greenhouse gas concentrations. The CESM preindustrial control runs for 160 years and the last 30 years of data are used for the analysis. For each experiment, the output includes monthly means of the model state and all terms in the momentum budget.

For the model comparison, we use a climatology based on the current velocity observed by acoustic Doppler current profiler on mooring array service cruises from Johnson et al. (2002). The data contain 10 longitudinal sections (143°E, 156°E, 165°E, 180°E, 170°W, 155°W, 140°W, 125°W, 110°W, and 95°W) with the depth deeper than 300 m during 1985–2000. The observation data were a key part of the World Ocean Circulation Experiment and the Tropical Ocean Global Atmosphere Coupled Ocean-Atmosphere Response Experiment (Eldin et al., 1994), primarily during the 1990s, see more details in Johnson et al. (2002).

3. Method

In the present study the zonal volume transport in the tropical Pacific is diagnosed using the method of Kessler et al. (2003). The time mean, vertically integrated momentum equations are as follows:

$$\frac{dU}{dt} + A^x - fV = -P_x + \tau^x + F^x \tag{1a}$$

$$\frac{dV}{dt} + A^y + fU = -P_y + \tau^y + F^y \tag{1b}$$

Where $\frac{d\vec{V}}{dt} = (\frac{dU}{dt}, \frac{dV}{dt})$, $\vec{A} = (A^x, A^y)$, $(-fV, fU)$, $\nabla\vec{P} = (P_x, P_y)$, $\vec{\tau} = (\tau^x, \tau^y)$, and $\vec{F} = (F^x, F^y)$ are the tendency of the horizontal ocean current, advection, Coriolis, horizontal pressure gradient, surface wind stress, and the friction terms, respectively.

In order to simplify the formulation, we use the method of Kessler et al. (2003) and treat the advection, friction, horizontal pressure gradient term, and the tendency of the horizontal ocean current as forcings, not only the surface wind stress. Then we may define a new forcing term as the generalized stresses $\tau^* = \tau + \tau' + \tau'' + \tau''' + \tau''''$, where $\tau' = -\vec{A}, \tau'' = \vec{F}, \tau''' = -\nabla\vec{P}, \tau'''' = -\frac{d\vec{V}}{dt}$. The momentum equations can be rewritten as follows.

$$-fV = \tau^{*x} \tag{2a}$$

$$fU = \tau^{*y} \tag{2b}$$

Taking the curl of equations (2a) and (2b) and considering the vertically integrated mean continuity equation ($U_x + V_y = \omega_{bot} - \omega_{top}$), we obtain the vorticity equation in a form similar to the classical Sverdrup balance, but with the surface wind stress replaced by τ^* defined above.

$$\beta V = \mathrm{curl}(\tau^*) \tag{3}$$

$$\mathrm{curl}(\tau^*) = \mathrm{curl}(\vec{\tau}) + \mathrm{curl}(-\vec{A}) + \mathrm{curl}(\vec{F}) + \mathrm{curl}(-\nabla\vec{P}) + \mathrm{curl}\left(-\frac{d\vec{V}}{dt}\right) - f\omega_{bot} \tag{4}$$

Theoretically, the $\mathrm{curl}(-\nabla\vec{P})$ and $\mathrm{curl}\left(-\frac{d\vec{V}}{dt}\right)$ should be zero and small for a long time average. However, these two terms are not zero because of (i) the model numerics (no-slip boundary conditions) at the eastern

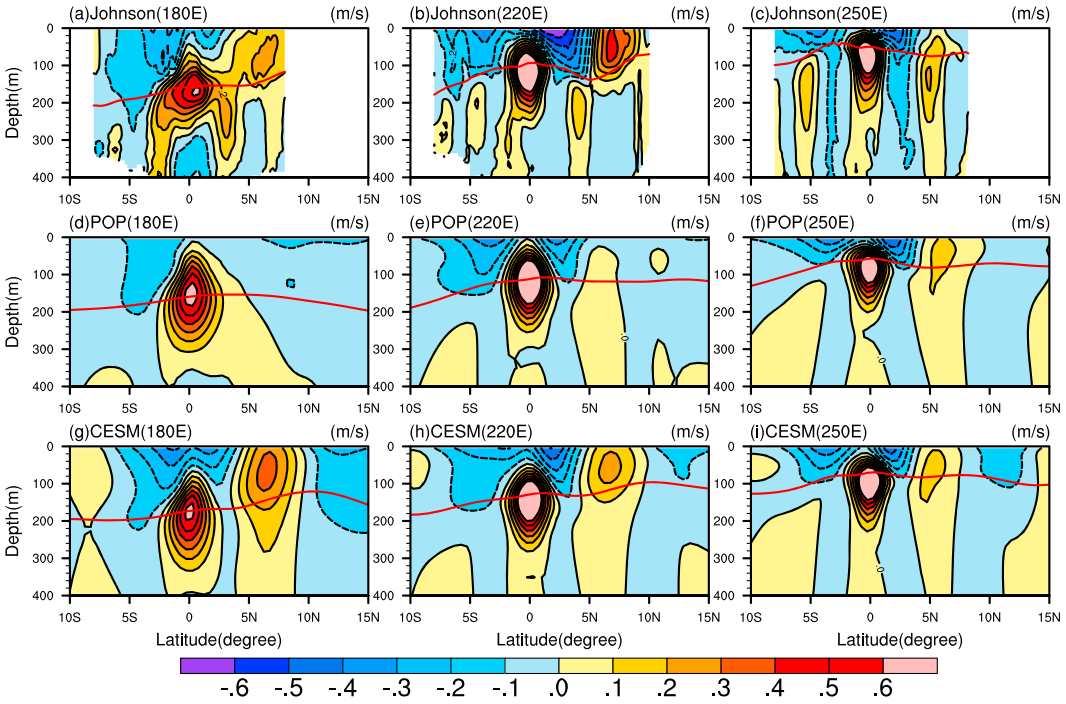

Figure 1. Meridional-vertical sections of annual mean zonal currents at (a) 180°E, (b) 220°E, and (c) 250°E for Johnson et al. (2002) observation. (d–f) and (g–i) are the same as (a–c) but for the POP and CESM experiments, respectively. The contour interval for all panels is 0.1 m/s. Eastward (westward) velocities are shown as solid (dashed) lines. The red curves are 20 °C isotherms. Unit: m/s. POP = Parallel Ocean Program; CESM = Community Earth System Model.

boundary of basins (Yeager, 2013) and (ii) the small interannual and decadal variability in the model, respectively. Then, the zonal transport, U, can be computed by zonally integrating the continuity equation from the eastern boundary and using (3).

$$U = -\frac{1}{\beta}\int_{EB}^{x} \mathrm{curl}\left(\tau^{*}\right)_{y} \mathrm{d}x + U_{EB} \tag{5}$$

Note that (5) ignores an additional term from taking the y derivative of β in (3), namely, the zonal integral of $\frac{1}{\beta^2}\,\mathrm{curl}\left(\tau^{*}\right)\frac{\partial \beta}{\partial y}$, but this term is $O(10^{-3})$ comparing with the main term $\frac{1}{\beta}\,\mathrm{curl}\left(\tau^{*}\right)_{y}$. Here, U_{EB} is the transport at the eastern boundary (EB). Practically, to avoid the uncertainties of the value of U_{EB}, the stream function form of (4) is used to compute U as Kessler et al. (2003). This leads to the following:

$$U = -\varphi_{y} \tag{6}$$

where $\varphi = \frac{1}{\beta}\int_{x(y)}^{x} \mathrm{curl}\left(\tau^{*}\right)\mathrm{d}x$ is the stream function of vertically integrated volume transport. The values of φ along the coast of the Americas are assigned to 0. Therefore, the zonal transport can be computed by (6) if the surface wind stress, the advection, and other terms are known. The surface wind stress term, advection term, friction term, and the horizontal pressure gradient term are accumulated each time step and saved as monthly averages.

Based on the observation in Figure 1 (top row), the vertical extent of the NECC is above 200 m in the western and central Pacific. In the eastern Pacific, the core of NECC can reach around 300 m. The current below 400 m is very weak. We chose 400 m as the integration depth, comparable with that used in Kessler et al. (2003; 353 m). We also have examined the integration of the upper 200 m for comparison, and the results were qualitatively similar.

4. Results

4.1. Modeled Biases in Simulating the NECC

Figure 1 shows the vertical-meridional sections of mean zonal current at three longitudes 180°E, 220°E, and 250°E, representing the western, central, and eastern equatorial Pacific, respectively. The observational climatology of Johnson et al. (2002) is used to compare with the POP and CESM experiments. At the surface, the eastward NECC is located between about 3°N and 10°N, just to the north of the South Equatorial Currents. The speed of the NECC is about 0.2, 0.4 and 0.2 m/s at these longitudes in the Johnson data, respectively. The eastward Equatorial Undercurrent (EUC) is below the surface along the equator. The center of EUC is strengthening and tilting up from the west to east as expected. The maximum velocity of EUC is approximately 0.6 m/s in the western Pacific and exceeds 1 m/s in the eastern equatorial Pacific. In the observations, two subsurface eastward jets on either side of the EUC, the North Subsurface Countercurrent and the South Subsurface Countercurrent (Wyrtki & Kilonsky, 1984), are seen in the western Pacific.

Compared against observation, the modeled NECC biases in the POP experiment are evidently with very weak current strength (Figures 1d–1f), similar to most of the model results shown in Tseng et al. (2016). The modeled NECC is weaker and closer to the equator at all longitudes. Almost no NECC core exists at the surface at 180°E, and the subsurface eastward jets are merged with the EUC. At 220°E, the simulated NECC is separated from the EUC but the main core still cannot be found near the surface. The core of the current is located at about 6°N with the magnitude of approximately 0.1 m/s. The modeled current speed is much weaker than the observed value of 0.4 m/s or larger. At 250°E, the NECC is evident at the surface with a magnitude comparable with the observation (about 0.1 m/s). The mean model currents during the period of the Johnson climatology data are almost identical with the model results of 30 years mean (1978–2007), indicating that the comparison between the Johnson data and the 30-year mean model results are not significantly affected by the interannual variability of the NECC.

The biases in both magnitude and location of the NECC are remarkably reduced in the CESM experiment. The simulated NECC is comparable with the observations in the central and eastern tropical Pacific (180°E and 250°E). The major difference between the CESM experiment and the observations occurs in the central Pacific, 220°E, particularly in the magnitude. Although the maximum velocity (between 0.1 and 0.2 m/s) of the NECC for the CESM experiment is higher than that for the POP experiment, it is still weaker than the observed 0.4 m/s.

To quantify the modeled NECC biases for these two simulations, the upper 400m vertically integrated zonal currents and the differences (CESM minus POP) in the equatorial Pacific are shown in Figures 2a–2c, respectively. This modeled zonal transport can be directly compared with the Sverdrup transport if the linear theory holds. The simulated NECCs are very different between the POP and the CESM experiments. The maximum transport of the NECC in the POP experiment is located mostly east of 150°W with the magnitude about 20 m^2/s, while the maximum transport of NECC in the CESM experiment is located in the western Pacific with the magnitude of over 60 m^2/s. To the west of 150°W, the eastward transport in the POP experiment moves southward to 5°N and merges with the strong eastward transport along the equator, the vertically integrated EUC. The shift of the NECC in the central equatorial Pacific is very similar to the results of Yu et al. (2000), but the gap is located further east. Yu et al. (2000) attributed this bias to the strong zonal wind at the equator.

The meridionally integrated eastward upper 400-m transports between 3°N and 10°N of NECC are further compared in Figure 2d for 10 observation sections from Johnson et al. (2002, black dots) and the simulations (solid curves). Meridional sections constructed from contemporaneous conductivity-temperature-depth and acoustic Doppler current profiler data taken across the Pacific, primarily during the 1990s, have been used in the construction of the Johnson climatology. The Johnson data set includes missing values at certain depths and latitudes where insufficient data was gathered to make a climatology, and there are only three longitudes (155°W, 140°W, and 125°W) with no missing values between 3°N and 10°N.

For better comparison between the Johnson climatology and the simulation results, we mask the model output with the same missing value locations as the Johnson climatology. The NECC transports from the masked model output are shown by the dashed lines in Figure 2d. The differences between the full and

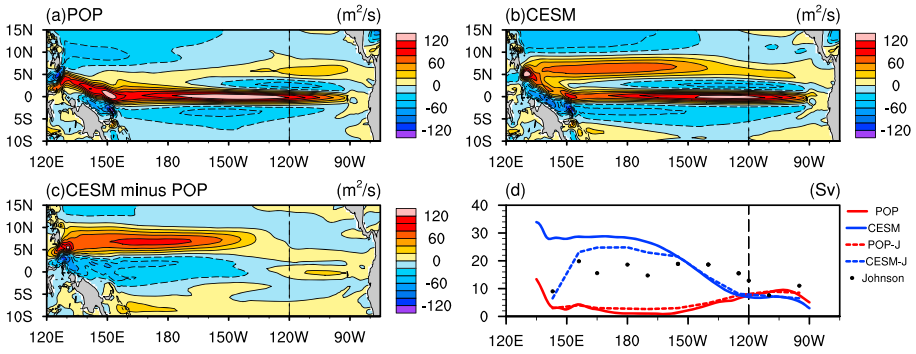

Figure 2. The upper 400m vertically integrated zonal currents (Units: m^2/s) for (a) POP with CORE-II forcing, and (b) CESM coupled model in the equatorial Pacific. (c) The upper 400m vertically integrated zonal current difference between the CESM and POP experiments. (d) The volume transports of the NECC (Unit: Sv), which are defined as the meridionally integrated upper 400m eastward transport between 3° and 10°N, for POP forced with CORE-II (red solid), CESM (blue solid) and Johnson et al. (2002) observation (black dots). The transports of the NECC masked by the observational sampling are also computed for both POP (red dash) and CESM (blue dash), donated as POP-J and CESM-J. CORE = Coordinated Ocean-ice Reference Experiments; NECC = North Equatorial Countercurrent; POP = Parallel Ocean Program; CESM = Community Earth System Model.

masked model analysis is small except for the section at 143°E, where the solid and dashed curves for the CESM experiment differ significantly, about 29.4 Sv for fully sampling and 6.5 Sv with masking based on the observations (135°E–150°E average). This suggests that insufficient sampling might lead to the underestimation of NECC transport at this section, so we will not consider it further in the present study.

Since Figure 2d suggests that the modeled biases to the west and east of 120°W behave differently, Table 1 further compares the observed volume transport to the west (17.4 Sv) and east (9.3 Sv) of 120°W, respectively, with the model results. West of 120°W, the overall NECC transport of the POP experiment is 2.9 Sv, significantly underestimating the observational value, while the transport in the CESM experiment is 21.7 Sv, an overestimate compared with the observations. East of 120°W, the overall NECC transport of 6.3 Sv in the CESM experiment is too weak but the NECC transport in the POP experiment (8.2 Sv) is much closer to the observations.

The above analysis shows large biases exist in simulating the NECC in the POP experiment, while the coupled CESM seems to produce much better agreement with the observed NECC in general. The biases are not homogenous across the basin. The POP experiment underestimates the NECC transport over most of the basin (west of 120°W), and CESM experiment underestimates it to the east of 120°W. In the next section, we will further analyze the dynamical mechanism leading to such a difference.

4.2. Contributions to the Zonal Transport Biases of NECC

To understand the causes of these zonal transport biases of the NECC shown in the POP and CESM experiments, we quantitatively diagnose the individual contributions resulting from the surface wind stress, the advection, the friction, and other terms based on the vorticity balance, following the method of Kessler et al. (2003; Figure 3). The sum of these four terms is exactly the total zonal transport shown in Figures 2a and 2b. Here the "other terms" are the sum of $\mathrm{curl}(-\frac{\mathrm{d}\vec{V}}{\mathrm{d}t})$, $\mathrm{curl}(-\nabla\vec{P})$, and $-f\omega_{400m}$, which are relatively small compared with the three main terms. The upper 400m integrated eastward zonal currents between 3° and 10°N from two experiments are overlaid as contours in Figure 3. For both CORE-II forced and coupled experiments, the patterns and magnitudes look similar between the wind stress term (Figures 3a and 3b) and the total transport (Figures 2a and 2b), confirming the key role of the wind stress on the NECC simulation. However, there are evident differences. The maximum zonal Sverdrup transport of the NECC due to

Table 1
The Zonal Averaged Volume Transport of NECC for Johnson et al. (2002) Climatology, POP, and CESM Experiments

	Total 150°E–270°E	West 150°E–240°E	East 240°E–270°E
Johnson	15.6	17.4	9.3
POP	4.2 (5.0)	2.9 (4.0)	8.2 (8.7)
CESM	17.8 (17.0)	21.7(20.0)	6.3 (6.9)

Note. The values in the parentheses are the transport of the North Equatorial Countercurrent sampled on the observational array positions. Units: Sv (10^6 m^3/s). POP = Parallel Ocean Program; CESM = Community Earth System Model.

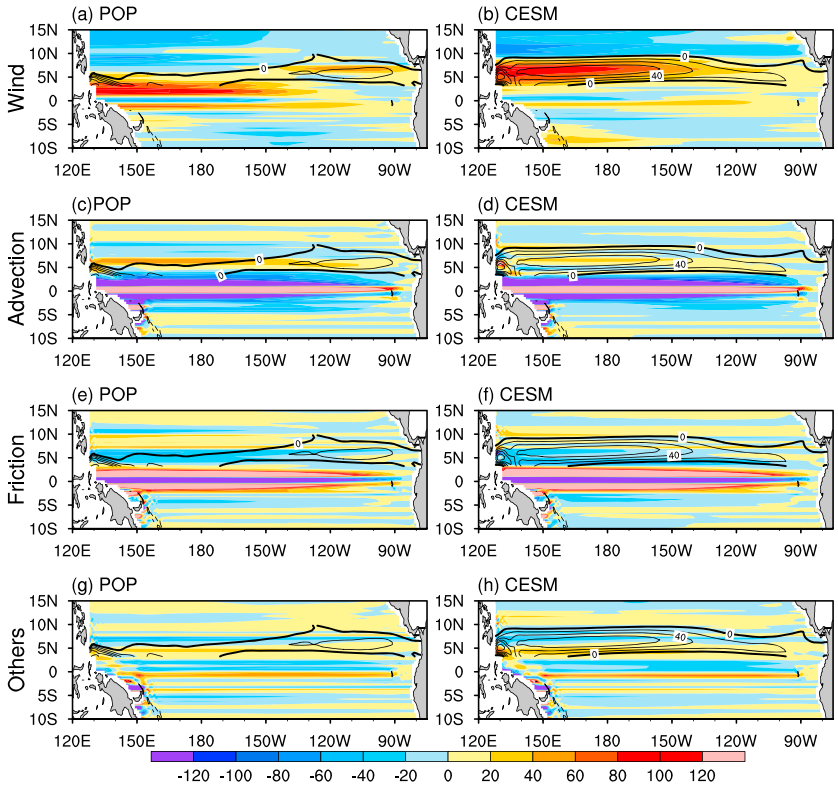

Figure 3. The zonal transport due to (a) wind stress, (c) advection, (e) friction, and (g) other terms in the tropical Pacific for POP. (b), (d), (f), and (h) are the same as (a), (c), (e) and (g), but for CESM. Unit: m^2/s. The contours are the eastward ocean current between 3° and 10°N for total transport which is shown in Figure 2a (for POP) and Figure 2b (for CESM). The contour interval is 20 m^2/s. The zero line is bolded. POP = Parallel Ocean Program; CESM = Community Earth System Model.

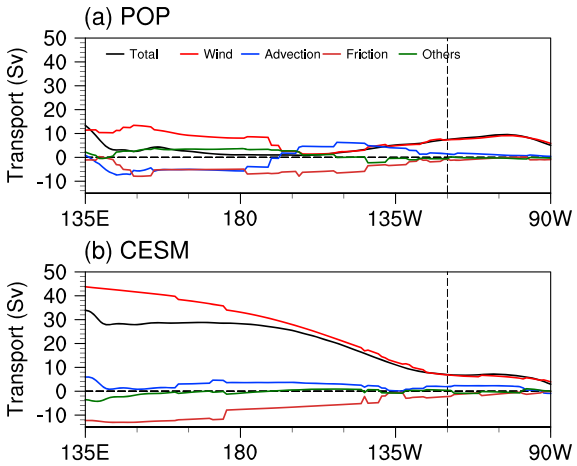

Figure 4. The total volume transports of NECC (black) and the transport due to wind stress (red), advection (blue), friction (brown), and other terms (green) for (a) POP and (b) CESM. Unit: Sv (10^6 m^3/s). NECC = North Equatorial Countercurrent; POP = Parallel Ocean Program; CESM = Community Earth System Model.

wind stress is larger than that of the total transport for both experiments, 40 Sv (wind) versus 20 Sv (total) for POP and 80 Sv (wind) versus 60 Sv (total) for CESM. We also find that the eastward transport resulting from the WSC exists in the western equatorial Pacific in the POP experiment (Figure 3a), but the location is too far south and close to the equator.

To better quantify these terms, Figure 4 compares these four contributions to the NECC transport with the total. Here a NECC "domain" is defined as the locations between 3°N and 10°N where the transport is eastward, which is shown within the contour in Figure 3. The total transport of the NECC is defined as the meridional-vertical integral of the ocean current in the NECC domain (i.e., the contribution at locations with westward current is set to zero). The other four terms are integrated in space over the same NECC domain, regardless of the sign of these terms within that domain.

The zonal NECC transports resulting from the four vorticity budget terms are relatively large in the western Pacific and small in the eastern Pacific in both experiments. To the east of 120°W, the zonal transport of the NECC resulting from the wind stress dominates the total transport in both experiments, 8.0 Sv for POP and 5.9 Sv for CESM. The transports resulting from the advection and other terms are all smaller than that of the wind stress (Table 2). These results suggest that the surface wind biases contribute to the underestimation of NECC transport to the east of 120°W in the CESM experiment.

Table 2
The Zonal Averaged Volume Transport of the NECC Due to Wind Stress, Advection, Friction, and Other Terms for the POP and CESM Experiments

	Total 150°E–270°E		West 150°E–240°E		East 240°E–270°E	
	POP	CESM	POP	CESM	POP	CESM
Wind	6.8	21.1	6.4	26.2	8.0	5.9
Advection	0.2	2.3	−0.1	2.6	1.1	1.6
Friction	−3.9	−5.5	−5.0	−7.0	−0.6	−1.0
Others	1.1	−0.1	1.6	0	−0.3	−0.2
Total	4.2	17.8	2.9	21.7	8.2	6.3

Note. The NECC transport is defined as the meridionally integrated eastward transport between 3°N and 10°N. Unit: Sv (10^6 m^3/s). NECC = North Equatorial Countercurrent; POP = Parallel Ocean Program; CESM = Community Earth System Model.

To the west of 120°W, the transport decompositions are more complicated. In POP the wind term is small and the magnitudes of friction and advection are comparable to the wind term (Figure 4), whereas the wind term in CESM is much larger than all other terms, with friction being the next most important term. Overall, it can be said that the weak transport of the NECC in the POP experiment comes mainly from the weak contribution of surface wind (6.4 Sv, weaker than the 26.2 Sv in CESM), see Figure 4 and Table 2. The NECC transport derived from the other terms is small in both models (Figure 4).

4.3. Differences in Wind Stresses and WSC

Section 4.2 suggests the key forcing role of the surface wind stress on simulating the NECC in both experiments. From the perspective of the contribution to zonal transport contribution (Figure 4), it is possible that the CORE-II wind stress used to force POP is more accurate than the wind stress in the CESM coupled simulation in the eastern equatorial Pacific (east of 120°W) and less accurate in the central western part (west to 120°W) of the basin. Therefore, we focus on the differences of the wind stress and the WSC between the two simulations in this subsection. The eastern and central western tropical Pacific will be discussed individually.

The mean zonal and meridional wind stresses are compared in Figure 5 for both experiments, and their differences (CESM minus POP) are also presented (bottom panel). Compared with CESM, the POP experiment's easterly trade winds are much stronger in the Northern Hemisphere west of 120°W, and the

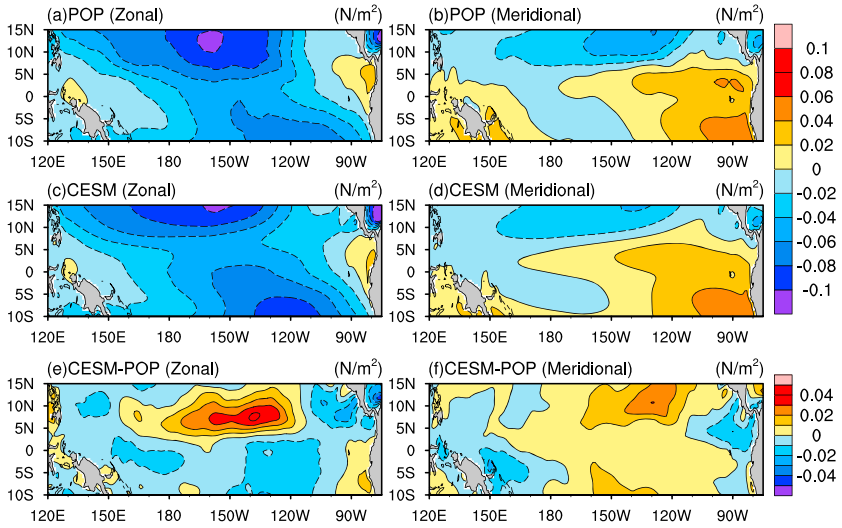

Figure 5. Mean zonal wind stress for (a) POP, (c) CESM, and (e) the difference between CESM and POP (CESM-POP). Panels (b),(d), and (f) are the same as (a), (c), and (e), but for meridional wind stress. Unit: N/m^2. POP = Parallel Ocean Program; CESM = Community Earth System Model.

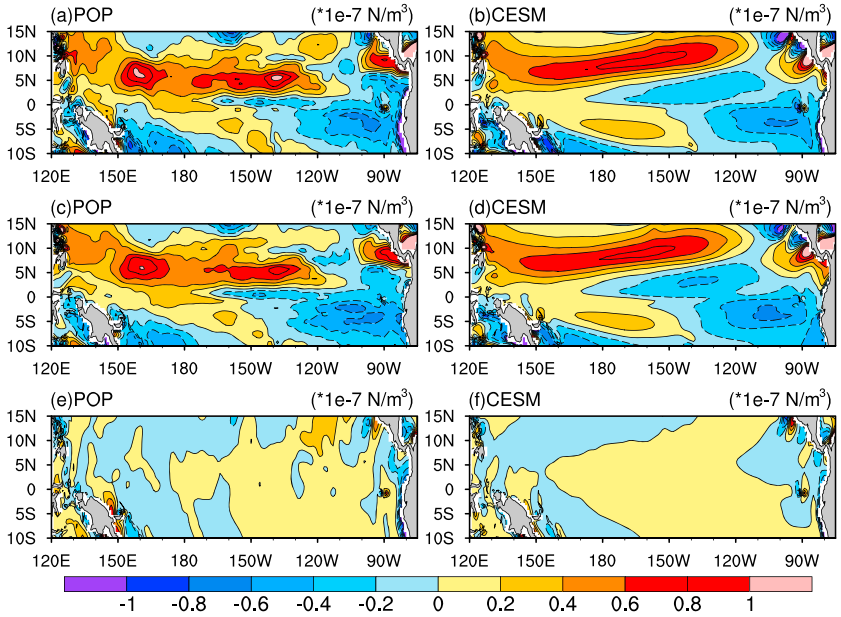

Figure 6. Mean (a) WSC, the WSC due to (c) the zonal ($-\frac{\partial \tau_x}{\partial y}$), and (e) the meridional ($\frac{\partial \tau_y}{\partial x}$) wind stresses for POP. Panels (b), (d), and (f) are the same as (a), (c), and (e), but for CESM. Unit: 10^{-7} N/m^3. WSC = wind stress curl; POP = Parallel Ocean Program; CESM = Community Earth System Model.

maximum of westward zonal wind stress shifts equatorward in the Northern Hemisphere (Figures 5a and 5c). The largest differences with a magnitude larger than 0.04 N/m^2 can be found between the dateline and 120°W in the latitude band 5°–10°N (Figure 5e).

In contrast, the zonal wind stress east of 120°W becomes weaker in the CORE-II forced experiment compared to CESM with a magnitude of about 0.02 N/m^2. There are some small structures along the coast of the Central America in the CESM experiment around 10°N (Figure 5c), which are absent in the POP experiment. This relates to the winds from the Atlantic to the Pacific through the three major gaps of the Central American cordillera: at the isthmus of Tehuantepec, over Lake Nicaragua, and at Panama (Xie et al., 2005).

The meridional wind stresses are weaker in the CESM experiment than in the CORE-II forced POP experiment by up to 0.03 N/m^2 in the region of northeasterlies around 10°N between the dateline and 100°W. Like the zonal component, there are also differences in small structures along the eastern boundary. The wind stress differences can help us to explain many differences in the WSC and their contribution on the transport of the NECC. Figure 6 shows the climatological mean WSC, and the individual contributions resulting from the zonal and meridional components in both experiments. It is clear to see the dominant role of zonal wind stress on the WSC over the whole region, while the meridional wind stress is only important along the eastern and western boundaries. These results are reflected in the Sverdrup transports calculated by these individual components (Figure 7).

We note the remarkably different patterns of positive WSC in the Northern Hemisphere between the POP and CESM experiments (Figures 6a and 6b). The positive WSC band is quite zonal with the maximum magnitude of 10^{-7} N/m^3 in the POP experiment. A similar band can be found in the CESM but it extends from southwest to northeast between 5°N and 15°N with slightly weaker magnitude. According to equation (5), the meridional derivative of the WSC, curl$(\tau)_y$, is the dominant term for the zonal Sverdrup transport. Therefore, the positive values of curl$(\tau)_y$ follows the southern edge of the positive WSC belt in Figure 6, which may contribute to the large zonal transport differences west of 120°W. The weaker NECC transport in the POP experiment than in the CESM experiment closely relates to the southward shift of the maximum easterly trade wind in the Northern Hemisphere.

In general, from (5), the part of the NECC zonal transport that results from the wind forcing will be strong when the second meridional derivative of the zonal stress is large and positive, and it is zonally coherent. In other words, the westward zonal stress must have a local minimum (i.e., a local maximum in the eastward

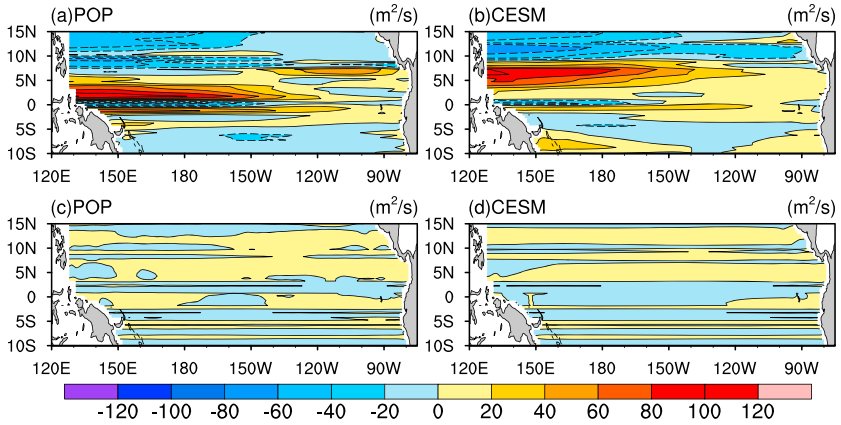

Figure 7. The zonal Sverdrup transport due to (a) zonal $(-\frac{\partial \tau_x}{\partial y})$ and (c) meridional $(\frac{\partial \tau_y}{\partial x})$ wind stresses for POP. Panels (b) and (d) are same as (a) and (c), but for CESM. Unit: m^2/s. POP = Parallel Ocean Program; CESM = Community Earth System Model.

stress) that spreads over a long zonal extent. This situation is set up naturally in the ITCZ and is seen, for example, in Figure 5c. However, if the minimum in westward stress occurs too close to the equator, as found in the POP simulation (Figure 5a), the curl-driven zonal transport is mixed up erroneously with the equatorial currents. It will be shown below that the wind corrections applied in the construction of the CORE are forcing increase to the westward wind stress in the NECC latitudes and forces the minimum too close to the equator.

Due to the northeasterly gap winds crossing the Central America and southerly winds crossing the equator, the biases east of 120°W are different from its western side. Figure 8 shows the mean wind stress vector (with the corresponding WSC superimposed) and the associated Sverdrup transport in this region. Negative (positive) WSC is formed on the northside (southside) of the northeasterly jets. The offshore positive WSC over 5°–10°N results from the competition between the northeasterly winds through the middle passage over Lake Nicaragua, and the southerly winds crossing the equator.

Comparing with the QuikSCAT product SCOW (the Scatterometer Climatology of Ocean Winds, Risien & Chelton, 2008; Figure 8a), the gap winds are poorly resolved in the CORE-II product, based on NCEP/NCAR reanalysis winds (resolution: 2.5°) and the WSC formed on the two sides of the northeasterly

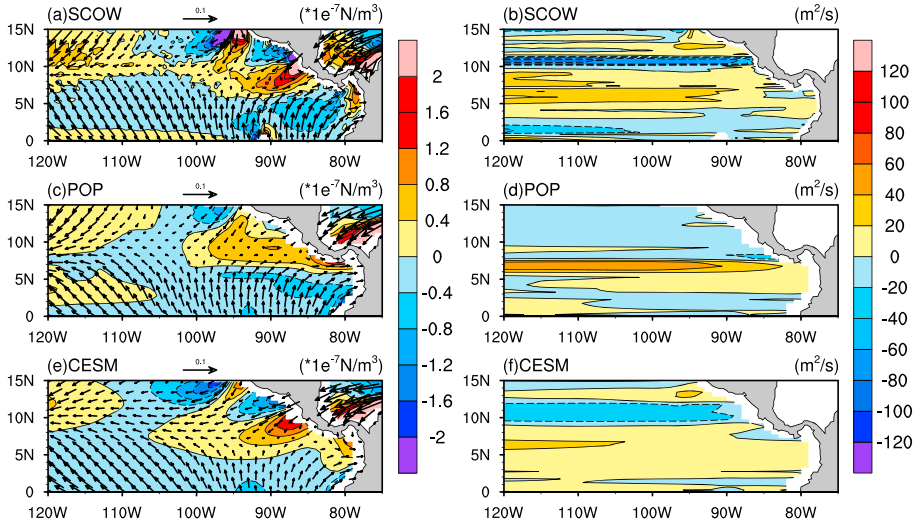

Figure 8. (a) The wind stress (vector), the WSC (shade), and (b) the associated zonal Sverdrup transport in the eastern equatorial Pacific for SCOW. Panels (c) and (d are same as (a) and (b), but for the POP experiment. Panels (e) and (f) are for the CESM experiment. The units are N/m^2, 10^{-7} N/m^3, and m^2/s for the wind stress, wind stress curl, and the Sverdrup transport, respectively. POP = Parallel Ocean Program; CESM = Community Earth System Model.

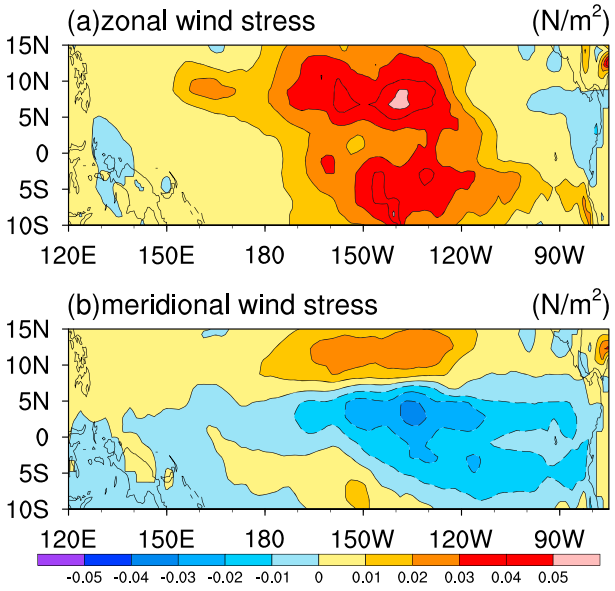

Figure 9. The differences of (a) zonal and (b) meridional wind stress between the uncorrected and corrected CORE-II data (uncorrected minus corrected). Unit: N/m^2. SCOW = Scatterometer Climatology of Ocean Winds; POP = Parallel Ocean Program; CESM = Community Earth System Model; CORE = Coordinated Ocean-ice Reference Experiments.

jets is very different to SCOW: the strength of WSC is weak and the direction of positive WSC is zonal. The CESM coupled model has higher resolution of these features than CORE-II forcing data and has gap wind and WSC pattern more similar to SCOW, but the magnitude is still weaker, which may be attributed to the unrealistic topography of the Central American cordillera. At the same time, the relatively weak cross-equatorial wind in CESM results in a small WSC gradient and thus the weak NECC in this region. The difference of gap wind and WSC pattern between the POP experiment and SCOW is bigger than between the CESM experiment and SCOW. The stronger Sverdrup transport of the POP experiment is a consequence of the steady westward accumulation of curl$(\tau)_y$ with longitude at around 7°N which is not physically realistic.

4.4. The Effects of Wind Correction in CORE-II Data Set

All of our above analyses indicate that the biases of the NECC transport in the POP experiment result primarily from the biases in the zonal winds of the CORE-II data set (Large & Yeager, 2004, 2009). Here the 6-hourly 10m winds from the NCAR/NCEP reanalysis version 1 have been corrected based on the QuikSCAT satellite winds. QuikSCAT estimates the equivalent 10m neutral wind (Chelton et al., 2001; Liu & Tang, 1996; Wentz & Smith, 1999), and so a possible source of error is that in CORE the NCEP/NCAR actual 10m winds are corrected toward QuikSCAT equivalent neutral 10m winds. Equivalent neutral 10m winds ($\overrightarrow{U}_{10n}$) are most commonly defined as the winds that would have occurred for a given stress if the air-sea interface was neutrally stable (no buoyancy stratification at surface: e.g., no air-sea potential temperature difference, and air humidity equal to saturated humidity at the sea surface temperature, see, e.g. Liu & Tang, 1996). The rationale for providing equivalent neutral 10m winds from satellite scatterometer is as follows: the scatterometer measures backscatter from surface capillary waves which closely depend on the surface stress; and equivalent neutral 10m winds have a direct, one-to-one relationship with surface stress (Kelly et al., 2001; Liu & Tang, 1996).

In regions of an unstable air-sea interface, including much of the global ocean, particularly in the Tropics (e.g., Warm Pool) and western boundary currents in winter, the equivalent neutral 10m winds are stronger than the actual winds, typically by a few tens of centimeters per second (Liu & Tang, 1996), but with stronger effects at very low wind speeds. Thus, by adjusting the NCEP/NCAR reanalysis actual winds toward the QuikSCAT neutral 10m wind product, the wind speed is spuriously increased in these unstable regions. The corrected winds are treated as "actual winds" when forcing ocean models, and thus may be too strong in these regions.

In addition, the surface stress is a function of the air-sea motion difference, also known as relative wind ($\overrightarrow{U}_{10n}-\overrightarrow{U_O}$). In other words $\overrightarrow{\tau}=\rho_a C_{DN}\left|\overrightarrow{U_{10n}}-\overrightarrow{U_O}\right|\left(\overrightarrow{U_{10n}}-\overrightarrow{U_O}\right)$ where ρ_a is the atmosphere density and C_{DN} is the neutral 10m drag coefficient. Hence, QuikSCAT measurements are affected by the difference between wind and ocean current. Further, many ocean models, including POP in these experiments, feed their surface current into the surface bulk flux calculations, and if the QuikSCAT data are used to correct the NCEP/NCAR 10m winds used for forcing, the ocean surface current effect on surface stress will be double counted.

Wu et al. (2012) argued that the surface wind biases from QuikSCAT yield weak NECC in their numerical experiments. We found that the differences in the Northern Hemisphere between the uncorrected and corrected surface wind of CORE-II (Figures 9a and 9b, uncorrected minus corrected) have a similar pattern to the differences between the CESM and the POP experiments (Figures 5e and 5f) west of 120°W. Many studies have found that QuikSCAT wind measurement accuracy will be degraded by rain (Draper & Long, 2004; Fore et al., 2014; Huddleston & Stiles, 2000; Portabella & Stoffelen, 2001; Stiles & Yueh, 2002; Weissman et al., 2002, 2012). Thus, the QuikSCAT winds to which the reanalysis winds are corrected in CORE-II may poorly capture the true stress and WSC in the ITCZ region. As mentioned in the previous subsection,

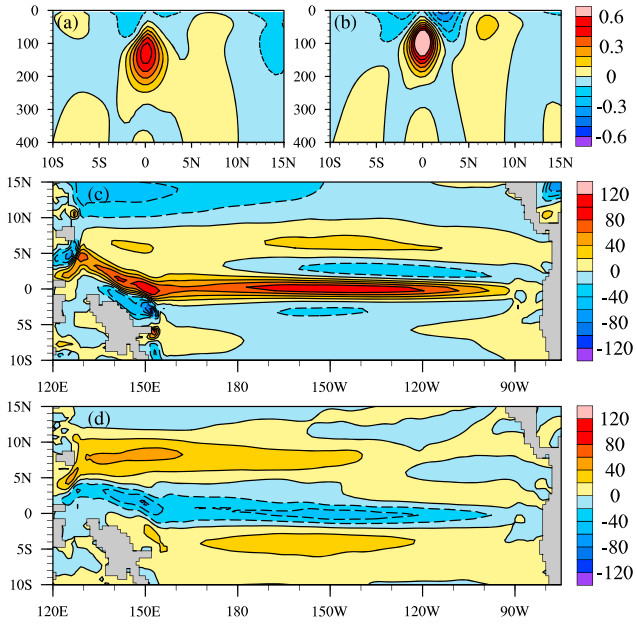

Figure 10. (a) Meridional-vertical sections of annual mean zonal currents at (a) 180°E, (b) 220°E for the POP-UNCO experiment. The contour interval for all panels is 0.1 m/s. Eastward (westward) velocities are shown as solid (dashed) lines. Unit: m/s. (c) the upper 400m integrated zonal currents (Unit: m^2/s) for the POP-UNCO experiment. (d) The upper 400m integrated zonal currents difference between the POP-UNCO and POP experiments. Unit: m^2/s.POP = Parallel Ocean Program; UNCO = Uncorrected.

when the CORE-II correction is made, the zonal stress is artificially increased in NECC latitudes (3°N–10°N), so that the minimum is shifted further south toward the equator (Figure 5a) and finally leads the reduction of the NECC.

To further investigate the impact of correcting the NCEP/NCAR reanalysis winds toward QuikSCAT, an additional numerical experiment (POP-UNCO) is analyzed, where wind correction has not been applied (see section 2). The meridional-vertical sections of annual mean zonal currents at 180°E, 220°E for the POP-UNCO experiment are shown in Figures 10a and 10b, respectively, together with upper 400m integrated zonal currents in Figure 10c and the upper 400m integrated zonal currents difference between the POP-UNCO and POP experiments in Figure 10d. Compared with the results of the POP experiment in Figures 1 and 2a, the POP-UNCO experiment has a stronger NECC in the western Pacific, which is also shown in Figure 10d. The average NECC transport between 150°E and 240°E is 7.6 Sv for POP-UNCO and 2.9 Sv for POP, respectively. The transport difference in Figure 10d is qualitatively similar to, but weaker than, that seen between CESM and POP, in Figure 2c. The difference in vorticity budget terms between POP-UNCO and POP was also found to be qualitatively similar to that between CESM and POP, with a dominance of WSC in driving the transport difference (not shown). The transports due to WSC in the western Pacific are 6.4 Sv for POP and 10.7 Sv for POP-UNCO, which contribute about 90% of the increase in the total transport. All the above results of the POP-UNCO experiment further suggest that the weak NECC in the CORE-II forced POP experiment derives from the correction to NCEP winds based on QuikSCAT.

It should be noted that in creating the recent JRA55-do ocean-forcing data set, based on JRA55 reanalysis, Tsujino et al. (2018) took into account the difference between equivalent neutral 10m winds and actual 10m winds due to air-sea stability (see Tsujino et al. for description of method). One of the consequences of this was weaker Tropical zonal trade winds than in CORE, more consistent with other data sets (Tsujino et al. 2018). However, preliminary experiments of POP forced with JRA55-do (not shown) also revealed weaker NECC than observed, and hence it may be inferred that the stability influence on the correction method on the NECC results is weak. In contrast the relative wind effect may be strong because of the presence of strong currents in a weak wind region. These equatorial zonal currents exhibit large gradients in the meridional direction, and as the zonal transport (5) depends on the meridional gradient of the curl of stress, which in turn is dominated by meridional gradient of the zonal component of stress, the surface currents may have a big effect. Current and future work of the authors is on investigating the influence of “relative wind” in sensitivity experiments in the CESM coupled and forced ocean model frameworks.

5. Summary

In the present study, the NECCs simulated by the CORE-II forced POP and the coupled CESM models have been investigated based on a modified Sverdrup balance approach proposed by Kessler et al. (2003). Comparing with the observations from Johnson et al. (2002), we found different model biases at the west/east of 120°W in simulating the NECC between the POP and CESM. The NECC transport is underestimated in POP west of 120°W, and it is underestimated in CESM east of 120°W.

Further analysis confirms that the surface wind stress and WSC is the most important forcing term for the NECC simulation in both models. West of 120°W, the NECC biases in the POP can be attributed to the southward movement of the maximum eastly trade winds in the north hemisphere, which mainly comes from the correction of NCEP/NCAR data to QuikSCAT equivalent neutral 10m winds. Indeed, the stronger NECC in POP-UNCO shows that some element of the correction method is to blame. East of 120°, the NECC biases in the CESM can be attributed to the weak cross-equatorial southerly winds and northeasterly gap

winds. For POP, the strong eastward transports are due to a chance zonal alignment of the poorly resolved WSC pattern.

Acknowledgments
We gratefully acknowledge Who Kim (NCAR) who advised us on running the uncorrected model and for general help with CESM. We gratefully acknowledge Greg Johnson for providing us access to the equatorial Pacific mean CTD/ADCP sections data in NetCDF (Johnson et al., 2002), which can be downloaded from https://floats.pmel.noaa.gov/gregory-c-johnson-home-page. Z. Sun, H. Liu, and P. Lin are supported by National Key R&D Program for Developing Basic Sciences (2016YFC1401401, 2016YFC1401601) and the National Natural Science Foundation of China (grants 41576025, 41576026, and 41776030). Y. Tseng is supported by the MOST106-2111-M-002-001 "Development and Validation of a New-generation, Fully-Coupled Global Climate System Model" and 107-2611-M-002-013-MY4 "Improving the Decadal Climate Prediction using a New Fully-Coupled Global Climate System Model". This study was also partially supported by the NSF Earth System Model (EaSM) grant 1419292 (EaSM-3: Collaborative Research: Quantifying Predictability Limits, Uncertainties, Mechanisms, and Regional Impacts of Pacific Decadal Climate Variability). J. Small is also supported by the NSF Earth System Model (EaSM) grant 1419292. F. Bryan is supported by NSF through its sponsorship of NCAR. The code of CESM2 can be downloaded from http://www.cesm.ucar.edu/models/cesm2/release_download.html. The model data used in this paper can be downloaded from https://pan.baidu.com/s/1eJSWwTCD4cc-7V9WRzx3Vg.

References

Chelton, D. B., Esbensen, S. K., Schlax, M. G., Thum, N., Freilich, M. H., Wentz, F. J., et al. (2001). Observations of coupling between surface wind stress and sea surface temperature in the eastern tropical Pacific. *Journal of Climate*, *14*(7), 1479–1498. https://doi.org/10.1175/1520-0442(2001)0142.0.CO;2

Clement, A. C., Seager, R., & Murtugudde, R. (2005). Why are there tropical warm pool? *Journal of Climate*, *18*(24), 5294–5311. https://doi.org/10.1175/JCLI3582.1

Danabasoglu, G., Yeager, S. G., Bailey, D., Behrens, E., Bentsen, M., Bi, D., et al. (2014). North Atlantic simulations in Coordinated Ocean-ice Reference Experiments phase II (CORE-II). Part I: Mean states. *Ocean Modelling*, *73*(1), 76–107. https://doi.org/10.1016/j.ocemod.2013.10.005

Donguy, J. R., & Meyers, G. (1996). Mean annual variation of transport of major currents in the tropical Pacific Ocean. *Deep Sea Research Part I Oceanographic Research Papers*, *43*(7), 1105–1122. https://doi.org/10.1016/0967-0637(96)00047-7

Draper, D. W., & Long, D. G. (2004). Evaluating the effect of rain on SeaWinds scatterometer measurements. *Journal of Geophysical Research*, *109*, C02005. https://doi.org/10.1029/2002JC001741

Eldin, G., Delcroix, T., Henin, C., Richards, K., du Penhoat, Y., Picaut, J., & Rual, P. (1994). Large-scale current and thermohaline structures along 156°E during the COARE intensive observation period. *Geophysical Research Letters*, *21*, 2681–2684. https://doi.org/10.1029/94GL01166

Fore, A. G., Stiles, B. W., Chau, A. H., Williams, B. A., Dunbar, R. S., & Rodríguez, E. (2014). Point-wise wind retrieval and ambiguity removal improvements for the QuikSCAT climatological data set. *Transactions on Geoscience and Remote Sensing*, *52*(1), 51–59. https://doi.org/10.1109/TGRS.2012.2235843

Gouriou, Y., & Toole, J. (1993). Mean circulation of the upper layers of the western equatorial Pacific Ocean. *Journal of Geophysical Research*, *98*, 22,495–22,520. https://doi.org/10.1029/93JC02513

Grima, N., Bentamy, A., Katsaros, K., Quilfen, Y., Delecluse, P., & Levy, C. (1999). Sensitivity of an oceanic general circulation model forced by satellite wind stress fields. *Journal of Geophysical Research*, *104*, 7967–7989. https://doi.org/10.1029/1999JC900007

Huddleston, J. N., & Stiles, B. W. (2000). A multidimensional histogram rain-flagging technique for SeaWinds on QuikSCAT. *International Geoscience & Remote Sensing Symposium*. https://doi.org/10.1109/IGARSS.2000.858077

Johnson, G. C., Sloyan, B. M., Kessler, W. S., & Mctaggart, K. E. (2002). Direct measurements of upper ocean currents and water properties across the tropical Pacific during the 1990s. *Progress in Oceanography*, *52*(1), 31–61. https://doi.org/10.1016/S0079-6611(02)00021-6

Kelly, K. A., Dickinson, S., Mcphaden, M. J., & Johnson, G. C. (2001). Ocean currents evident in satellite wind data. *Geophysical Research Letters*, *28*, 2469–2472. https://doi.org/10.1029/2000GL012610

Kessler, W. S., Johnson, G. C., & Moore, D. W. (2003). Sverdrup and nonlinear dynamics of the Pacific equatorial currents. *Journal of Physical Oceanography*, *33*(5), 994–1008. https://doi.org/10.1175/1520-0485(2003)0332.0.CO;2

Kistler, R., Collins, W., Saha, S., White, G., Woollen, J., Kalnay, E., Chelliah, M., et al. (2001). The NCEP–NCAR 50–year reanalysis: Monthly means CD-ROM and documentation. *Bulletin of the American Meteorological Society*, *82*(2), 247–267. https://doi.org/10.1175/1520-0477(2001)082<0247:TNNYRM>2.3.CO;2

Large, W. G., & Yeager, S. G. (2004). Diurnal to decadal global forcing for ocean and sea-ice models: The data sets and flux climatologies. NCAR Technical Note NCAR/TN-460+STR. https://doi.org/10.5065/D6KK98Q6

Large, W. G., & Yeager, S. G. (2009). The global climatology of an interannually varying air–sea flux data set. *Climate Dynamics*, *33*(2–3), 341–364. https://doi.org/10.1007/s00382-008-0441-3

Liu, W. T., & Tang W. (1996). Equivalent neutral wind, JPL Publication 96–17, Jet propulsion Laboratory, Pasadena, 16 pp.

Masunaga, H., & L'Ecuyer, T. S. (2011). Equatorial asymmetry of the East Pacific ITCZ: Observational constraints on the underlying processes. *Journal of Climate*, *24*(6), 1784–1800. https://doi.org/10.1175/2010JCLI3854.1

Meyers, G., & Donguy, J. R. (1984). The North Equatorial Countercurrent and heat storage in the western Pacific Ocean during 1982–83. *Nature*, *312*(5991), 258–260. https://doi.org/10.1038/312258a0-260

Philander, S. G. H., Hurlin, W. J., & Seigel, A. D. (1987). Simulation of the seasonal cycle of the Tropical Pacific Ocean. *Journal of Physical Oceanography*, *17*(11), 1986–2002. https://doi.org/10.1175/1520-0485(1987)017<1986:SOTSCO>2.0.CO;2

Picaut, J., & Delcroix, T. (1995). Equatorial wave sequence associated with warm pool displacement during the 1986–1989 El Niño-La Niña. *Journal of Geophysical Research*, *18*, 1171–1183. https://doi.org/10.1175/1520-0426(2001)018<1171:RDAQCO>2.0.CO;2

Portabella, M., & Stoffelen, A. (2001). Rain detection and quality control of sea winds. *Journal of Atmospheric and Oceanic Technology*, *18*(7), 1171–1183. https://doi.org/10.1175/1520-0426(2001)018<1171:RDAQCO>2.0.CO;2

Richards, K., Xie, S.-P., & Miyama, T. (2009). Vertical mixing in the ocean and its impact on the coupled ocean/atmosphere system in the eastern tropical Pacific. *Journal of Climate*, *22*(13), 3703–3719. https://doi.org/10.1175/2009JCLI2702.1

Risien, C. M., & Chelton, D. B. (2008). A global climatology of surface wind and wind stress fields from eight years of QuikSCAT scatterometer data. *Journal of Physical Oceanography*, *38*(11), 2379–2413. https://doi.org/10.1175/2008JPO3881.1

Stiles, B. W., & Yueh, S. H. (2002). Impact of rain on spaceborne Ku-band wind scatterometer data. *Transactions on Geoscience & Remote Sensing*, *40*(9), 1973–1983. https://doi.org/10.1109/TGRS.2002.803846

Sverdrup, H. U. (1947). Wind-driven currents in a baroclinic ocean; with application to the equatorial currents of the eastern Pacific. *Proceedings of the National Academy of Sciences of the United States of America*, *33*(11), 318–326. https://doi.org/10.1073/pnas.33.11.318

Tseng, Y. H., Lin, H., Chen, H. C., Thompson, K., Bentsen, M., Böning, C. W., Bozec, A., et al. (2016). North and equatorial Pacific Ocean circulation in the CORE-II hindcast simulations. *Ocean Modelling*, *104*, 143–170. https://doi.org/10.1016/j.ocemod.2016.06.003

Tsujino, H., Urakawa, S., Nakano, H., Small, R. J., Kim, W. M., Yeager, S. G., Danabasoglu, G., et al. (2018). JRA-55 based surface dataset for driving ocean–sea-ice models (JRA55-do). *Ocean Modelling*, *130*, 79–139. https://doi.org/10.1016/j.ocemod.2018.07.002

Weissman, D. E., Bourassa, M. A., & Tongue, J. (2002). Effects of rain rate and wind magnitude on seawinds scatterometer wind speed errors. *Journal of Atmospheric and Oceanic Technology*, *19*(5), 738–746. https://doi.org/10.1175/1520-0426(2002)019<0738:eorraw>2.0.co;2

Weissman, D. E., Stiles, B. W., Hristova-Veleva, S. M., Long, D. G., Smith, D. K., Hilburn, K. A., & Jones, W. L. (2012). Challenges to satellite sensors of ocean winds: Addressing precipitation effects. *Journal of Atmospheric and Oceanic Technology*, *29*, 356–374. https://doi.org/10.1175/ JTECH-D-11-00054.1

Wentz, F. J., & Smith, D. K. (1999). A model function for the ocean-normalized radar cross section at 14 ghz derived from NSCAT observations. *Journal of Geophysical Research*, *104*, 11,499–11,514. https://doi.org/10.1029/98JC02148

Wu, F., Lin, P., & Liu, H. (2012). Influence of a southern shift of the ITCZ from quick scatterometer data on the Pacific North Equatorial Countercurren. *Advances in Atmospheric Sciences*, *29*(6), 1292–1304. https://doi.org/10.1007/s00376-012-1149-1

Wyrtki, K., & Kendall, R. (1967). Transports of the Pacific equatorial countercurrent. *Journal of Geophysical Research*, *72*, 2073–2076. https://doi.org/10.1029/JZ072i008p02073

Wyrtki, K., & Kilonsky, B. (1984). Mean water and current structure during the Hawaii-to-Tahiti shuttle experiment. *Journal of Physical Oceanography*, *14*(2), 242–254. https://doi.org/10.1175/1520-0485(1984)0142.0.CO;2

Xie, S. P., Xu, H., Kessler, W. S., & Nonaka, M. (2005). Air Sea interaction over the eastern Pacific warm pool: Gap winds, thermocline dome, and atmospheric convection*. *Journal of Climate*, *18*(1), 5–20. https://doi.org/10.1175/JCLI-3249.1

Yeager, S. G. (2013). Understanding and predicting changes in North Atlantic sea surface temperature. *Dissertations & Theses - Gradworks*.

Yu, Z., Mccreary, J. P. Jr., Kessler, W. S., & Kelly, K. A. (2000). Influence of equatorial dynamics on the Pacific North Equatorial Countercurrent. *Journal of Physical Oceanography*, *30*(12), 3179–3190. https://doi.org/10.1175/1520-0485(2000)0302.0.CO;2